Fast and slow axonal transport: A unified approach based on cargo and molecular motor coupled dynamics

Alexandre Y. C. Cho ⊙

Instituto de Física, Universidade de São Paulo, Rua do Matao, 05508-090 São Paulo, São Paulo, Brazil

Victor R. C. Mourão Roque ⊙[*]

Instituto de Ciência e Tecnologia, Universidade Federal de Alfenas, Rodovia José Aurélio Vilela 37715-400 Poços de Caldas, Minas Gerais, Brazil

Carla Goldman ⊙[†]

Instituto de Física, Universidade de São Paulo, Rua do Matao 05508-090 São Paulo, São Paulo, Brazil

The origins of the large differences observed in the rates at which diverse particles are conveyed along axonal microtubules are still a matter of debate in the literature. There is evidence that certain neurodegenerative diseases may be triggered by disturbances in the related transport processes. Motivated by this, we employ a model to investigate mobility properties of certain cargoes whose dynamics are coupled with that of molecular motors on crowded microtubules. For certain initial and boundary conditions, we use the method of characteristics to resolve perturbatively the pair of equations of Burgers type resulting from a mean-field approach to the original microscopic stochastic model. Extensions to nonperturbative limits are explored numerically. In this context, we are able to figure out conditions under which the cargoes' average velocities may differ up to orders of magnitude just by changing the number of motors on the considered track. We then discuss possibilities to connect these theoretical predictions with available experimental data about axon transport.

I. INTRODUCTION

The diverse types of particles that are usually transported along axons can be grouped into two major categories characterized by the average speed v at which this transport is put into effect. The group of fast-moving particles with $v \sim 0.5$–5.0 μm/s comprises membranous organelles such as the Golgi-derived vesicles, mitochondria, endosomes, and lysosomes, among others. The groups of slow-moving particles with $v \sim 0.003$–0.030 μm/s for slow component a (SCa) and $v \sim 0.02$–0.09 μm/s for slow component b (SCb) comprise nonmembranous neurofilaments, cytoskeletals, and cytosolic proteins, among others.

The general biological interest of related studies relies on the fact that certain neurological diseases are believed to be directly associated with failures of the system to keep the transport at the right rates leading, eventually, to local particle accumulation [1]. The review of Roy [2] offers a historical account of experimental achievements in this field and of the major hypotheses in the literature to explain the huge differences in the rates of particle transport along axons. One of the first models used in these studies, the dynamic recruitment model proposed to explain the slow movement, requires the presence of a common carrier structure [3,4] or even fast-moving cargo vesicles [5] to which cytosolic proteins would

transiently get attached. The slow rate with which these proteins are conveyed along the axon would then be attributed to the relatively large intervals of time along which they stay detached from the carrier [6]. A stochastic model accounting for these ideas is considered in [7]. The other major hypothesis, the stop and go model, attributes the causes of slow movement to the ability of neurofilaments, for example, to pause during transit. The duration of such pauses would be a determinant of the resulting slow rates, although their origins and eventual mechanisms of control still need clarification.

Evidence indicating that individual cytoskeletal polymers conveyed by slow transport in axons can also move as fast as membranous organelles suggests that both fast and slow transport in axons may be due to a single mechanism. Actually, a unified view of axonal transport had already been proposed by Ochs [8], according to which the only actual directed movement would be that of fast cargoes and the detected slow movement would be due to local and casual rearrangements of particles, not resulting in long-range transport. In line with this, it is argued these days that such a unified mechanism is supported by the dynamics of molecular motors and their ability to transport a variety of particles, referred to generically as cargoes, as they move on structured "tracks," i.e., along axonal microtubules [9]. However, one still may question the specific motors that would drive cargoes at such slow rates as shown by SCa and SCb [1]. In view of this, we believe that although the description based on molecular motors seems promising, it requires complement by mechanisms that regulate cargo-motor interactions, able to explain such

---
[*]victor.roque@unifal-mg.edu.br
[†]carla@if.usp.br

huge differences between the rates of slow and fast transport in the absence of a putative carrier. Our intention here is to contribute in this regard.

To that end, we investigate specific properties of a stochastic model proposed elsewhere [10–12]. It is conceived from the idea that the transport of cargoes by molecular motors is based on a mechanism of cargo hopping among motors which in turn depends crucially on the number of motors available on the track. Here we seek quantitative predictions for the cargoes' average velocities under these conditions. We explore situations under which motor congestion may actually act to promote cargo transport.

We should remark that there are always two main aspects concerning the dependence of cargo transport on molecular motors in such systems. One of these is related to the microscopic mechanisms of motor-cargo binding affinity. The other concerns the dependence of the transport on the number of available motors on the track, not only on the type of motor directly bound to each cargo [13–15]. In order to investigate the dependence on motor occupation on the track, we base our quantitative analysis on a model that describes the microscopic dynamics of motors and cargoes coupled through stochastic processes of asymmetric simple exclusion process (ASEP) type. The model embodies two microscopic mechanisms for cargo movement. One of these describes the movement of cargo while bound to a motor; the other describes cargo hopping between pairs of neighboring motors on a track. There is only one type of motor with bias in a definite direction; without prejudice for the analysis, this is defined anterograde. We have already studied the possibility of observing bidirectional movement in similar model systems [10–12]. The main concern of the present study is related to quantitative estimations for the average velocities developed by cargoes subject to these two mechanisms. We show conditions under which the average cargo speed may vary up to orders of magnitude simply by adjusting the number of motors available on axons. These results may be promising in offering possibilities to understand the differences observed in the rates of transport depicted by real axons in quantitative terms and under a unified perspective.

In Sec. II we derive the mean-field equations for the model. The resulting nonlinear coupled equations of Burgers type is studied analytically in the Appendix for certain initial and boundary conditions using the method of characteristics. As we will show, such solutions to this particular system of equations are achieved under a perturbative approximation. The analytical expressions obtained in this way indicate the relevant regions of parameters and particular initial and boundary values illustrating the role of each mechanism in producing such differences in the average cargo velocities, as observed. For more general conditions, away from the perturbative limits, we base our analysis on a numerical study to resolve the particular system of nonlinear equations of interest [16], explained in Sec. III. The results are discussed in Sec. IV. We summarize and discuss our conclusions in Sec. V.

II. CARGO HOPPING MODEL

The kind of ASEP model we will consider to describe the stochastic dynamics of molecular motors and cargoes has already been proposed elsewhere to study the so-called bidirectional movement [10–12]. The model version analyzed here embraces both mechanisms of cargo transport at the microscopic level, namely, the isolated motion of a cargo attached to a motor and also the mechanism of cargo hopping from motor to motor. The idea is to circumvent difficulties for long-range cargo transport due to motor jamming (congestion) on axons [17]. Accordingly, an axonal track is represented by a one-dimensional lattice whose sites may be occupied at each time either by an unloaded motor or by a loaded motor or else it can be empty. The model is defined by the dynamics of occupation, as follows:

$$
\begin{aligned}
10 &\rightarrow 01 \quad \text{with probability } p \quad [\text{process (a)}], \\
20 &\rightarrow 02 \quad \text{with probability } q \quad [\text{process (b)}], \\
12 &\rightarrow 21 \quad \text{with probability } f \quad [\text{process (c)}], \\
12 &\rightarrow 12 \quad \text{with probability } g \quad [\text{process (d)}].
\end{aligned}
\tag{1}
$$

Label 0 is assigned to an empty site. Label 1 is assigned to a site that is occupied by a motor carrying no cargo: an unloaded motor. Label 2 is assigned to a site occupied by a motor attached to a cargo: a loaded motor.

The pairs shown in (1) indicate that each of the possible processes is represented by the occupation of two neighboring sites. The parameters p, q, f, and g are the probabilities for the occurrence of each process per time interval Δt. Process (a) represents an elementary movement of a biased motor from the cell body towards the axon's terminal (anterograde direction). Process (b) represents an elementary process of the kind considered in (a) of a motor when carrying a cargo particle. The remaining processes describe the exchange of cargoes between neighboring motors, either to the left (c) or to the right (d). A condition for processes (a) and (b) to take place is that the site to the right of the motor remains empty during the time interval Δt. The two processes of exchange depend on the presence of a free motor to the right (c) or to the left (d) of the one attached to the cargo.

Continuous limit and mean-field approximation

In order to obtain the mean-field equations corresponding to processes (1) for continuous-time and space intervals, we follow the procedure described in [18] that nevertheless accounts only for one type of particle. In order to extend it to take into account the two types of particles present in our model, we define the vector

$$
P^t[n_1, n_2, n_3, \ldots, n_i, n_{i+1}, \ldots, n_{i+k}, \ldots, n_N].
\tag{2}
$$

For any $n_j = \{0, 1, 2\}$, $j = 1, \ldots, N$, it represents the probability of any configuration of particles and holes occupying the sites of the one-dimensional lattice at time t. The marginal probabilities are defined accordingly,

$$
P_i^t[n_i, n_{i+1}, \ldots, n_{i+k}] = \sum_{\substack{\{n_j\} \\ (1 \leqslant j < i;\, i+k < j \leqslant N)}} P^t[n_1, n_2, n_3, \ldots, n_i, n_{i+1}, \ldots, n_{i+k}, \ldots, n_N],
\tag{3}
$$

where N is the total number of lattice sites. With this, we represent the average densities of particles 1 and 2 at each site i by

$$\rho_i^t[1] = P_i^t[1]/N, \quad \rho_i^t[2] = P_i^t[2]/N. \tag{4}$$

The temporal behavior of the density at any site i can now be evaluated by relating it to the incoming flux of particles into that site, observing the processes defined through (1), as

$$\frac{1}{\Delta t}(P_i^{t+\Delta t}[1] - P_i^t[1]) = \frac{1}{\Delta t}\left\{ pP_{i-1}^t[10] - pP_i^t[10] + gP_i^t[21] - gP_{i-1}^t[21] + fP_{i-1}^t[12] - fP_i^t[12]\right\} \tag{5}$$

and

$$\frac{1}{\Delta t}(P_i^{t+\Delta t}[2] - P_i^t[2]) = \frac{1}{\Delta t}\left\{ qP_{i-1}^t[20] - qP_i^t[20] + gP_{i-1}^t[21] - gP_i^t[21] + fP_i^t[12] - fP_{i-1}^t[12]\right\}. \tag{6}$$

The mean-field approximation consists in neglecting correlations by taking, for example,

$$P_{i-1}^t[20] = \left(P_{i-1}^t[2]P_i^t[0]\right)/N,$$
$$P_i^t[21] = \left(P_i^t[2]P_{i+1}^t[1]\right)/N \tag{7}$$

and analogous expressions for the remaining two-point probability vectors. With these, we write

$$\frac{1}{\Delta t}\left(P_i^{t+\Delta t}[1] - P_i^t[1]\right) = \frac{l}{\Delta t}\left(-\frac{p}{Nl}\Delta_i\left(P_i^t[1]P_{i+1}^t[0]\right) + \frac{g}{Nl}\Delta_i\left(P_i^t[2]P_{i+1}^t[1]\right) - \frac{f}{Nl}\Delta_i\left(P_i^t[1]P_{i+1}^t[2]\right)\right),$$
$$\frac{1}{\Delta t}\left(P_i^{t+\Delta t}[2] - P_i^t[2]\right) = \frac{l}{\Delta t}\left(-\frac{q}{Nl}\Delta_i\left(P_i^t[2]P_{i+1}^t[0]\right) + \frac{f}{Nl}\Delta_i\left(P_i^t[1]P_{i+1}^t[2]\right) - \frac{g}{Nl}\Delta_i\left(P_i^t[2]P_{i+1}^t[1]\right)\right), \tag{8}$$

where the notation Δ_i on the right-hand side indicates the difference between the product inside the parenthesis and an analogous one obtained by shifting $i \to i-1$. Using that $P_i^t[0] = 1 - P_i^t[1] - P_i^t[2]$ and taking the continuous limit for which both the length l of the lattice sites and $\Delta t \to 0$, the two expressions become

$$\frac{\partial u}{\partial t} = -\alpha\frac{\partial}{\partial z}[u(1-u) - \theta(uc)],$$
$$\frac{\partial c}{\partial t} = -\beta\frac{\partial}{\partial z}[c(1-c) - \eta(uc)]. \tag{9}$$

This system of quasilinear hyperbolic equations describes the coupled dynamics of both quantities of interest, namely, the local density of free motors (i.e., motors that are not attached to cargoes) defined accordingly as

$$u(z,t) = \lim_{il \to z, l \to 0, N \to \infty} \frac{P_i^t[1]}{N}$$

and the local density of motors transiently attached to cargoes

$$c(z,t) = \lim_{il \to z, l \to 0, N \to \infty} \frac{P_i^t[2]}{N}$$

at each time t and position z of the axon. From now on, we will refer to $c(z,t)$ simply as the cargo density and to $u(z,t)$ as the motor density. The parameters α, β, θ, and η introduced above are defined in terms of parameters of the original stochastic (microscopic) model as

$$\alpha = p\xi, \quad \beta = q\xi,$$
$$\theta = \frac{p - (f - g)}{p}, \quad \eta = \frac{q + (f - g)}{q}, \tag{10}$$

where $\xi = \lim_{\Delta t \to 0; l \to 0} l/\Delta t$ is the scale.

The pair of hyperbolic coupled equations derived above (9) are of Burgers type. Due to the complexity of the mathematical problem, we consider certain initial and boundary values

that allow for analytical solutions using the method of characteristics [19,20]. It is then possible to demonstrate that for small differences between the numbers of cargoes and motors distributed along the track at initial times and for a broad range of numerical values for the model parameters (Table I), the system engenders two distinct values for the average velocities attained by wavelike profiles of cargo density that may differ by orders of magnitude. This suggests a quantitative relationship with the corresponding quantities measured in fast and slow axonal transport modes [2]. These solutions to the system (9), for the chosen initial and boundary conditions, are presented in the Appendix within a perturbative approach.
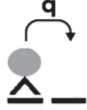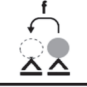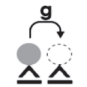
III. NUMERICAL STUDY

The results shown in the Appendix for the behavior of both motor and cargo densities achieved analytically for certain initial and boundary conditions are limited to situations for which shocks among characteristic lines and rarefaction regions are either absent or can be neglected within the considered perturbative limit. Because of this, numerical simulations have been performed in parallel to study the temporal behavior of $u(z,t)$ and $c(z,t)$. The aim is to extend the scope of applications, attempting to approach more closely the available data on axonal transport. In this section we briefly discuss some features of the numerical code developed to this end.

The nonlinearity of the set of equations (9) can create solutions with both discontinuities and small-scale smooth structures. These features, together with the expectation that the system develops velocities at very different orders of magnitude, led us to choose, from the many numerical methods available, a finite difference (FD) with a high-resolution shock-capturing (HRSC) scheme, widely used in astrophysical and cosmological codes [21–23].

The FD method has been chosen since it does not require the solutions of Riemann problems at each interface between

TABLE I. Model parameters: (a) parameter identification, (b) meaning, (c) possible relationship with the biological system, and (d) diagram of the microscopic process.

(a)	(b)	(c)	(d)
p	jumping probability (anterograde) unloaded motor	motor/track interaction	
q	jumping probability (anterograde) loaded motor	motor/track interaction	
f	cargo jumping probability (retrograde direction)	motor/cargo attach/detach	
g	cargo jumping probability (anterograde direction)	motor/cargo attach/detach	
ξ	speed scale	-	-
$\alpha = p\xi = \gamma + \varepsilon$	scaled parameter	-	-
$\beta = q\xi = \gamma - \varepsilon$	scaled parameter	-	-
ε/γ	small parameter	-	-
l	lattice space	motor step size	-
h	excess motor density on track at initial time	-	-
$x(z,t)$	excess motor density on position z of the track at time t	-	-
$y(z,t)$	excess cargo density on position z of the track at time t	-	-
$x_r = x(0,t)$	excess motor density at reservoir	-	-
$y_r = y(0,t)$	excess cargo density at reservoir	-	-

computational cells [16], reducing in this way time costs in comparison to the time used in performing the conventional finite-volume method. The HRSC method offers a high order of accuracy, sharp descriptions of discontinuities, and convergence to the physically correct solution. It has the advantage of treating discontinuous solutions consistently and automatically wherever they appear in the flow [24].

In this work we implement our own numerical code using modern FORTRAN with a modular approach. The code uses up to fifth-order reconstruction in the characteristic fields and a local Lax-Friedrichs flux splitting [25]. For a reconstruction scheme, we implement the classic weighted essentially nonoscillatory (WENO) schemes with third-order (WENO3) and fifth-order (WENO5) [16,26] and two different improved methods, a third-order WENO3p [27] and a fifth-order WENO5Z [28]. In addition to the aforementioned references, a brief and practical explanation of these methods can be found in Ref. [23]. The time integration of the ordinary differential equations obtained from the discretization of Eqs. (9) is made using a third-order strong stability-preserving Runge-Kutta scheme [29].

In order to ensure accuracy in the implementation of the code, we first wrote it for the classical Euler equations to run some of the usual validation tests. We then performed a few minor changes to fit the code for our purposes. Figure 1

depicts the results for the density curves obtained from three different tests and corresponding reconstruction schemes. In Fig. 1(a) we show the Sod test [30] evolved up to the time $t_{\text{end}} = 0.2$ with 100 cells. This test does not impose significant computational difficulties. Analytical solutions to the equations allow us to check for the accuracy with which the discontinuities are described by the implemented schemes. The blast wave considered in the second test [Fig. 1(b)] has been evolved up to $t_{\text{end}} = 0.015$ also with 100 cells. This is a stronger test because the initial profile presents a gradient of five orders of magnitude in pressure. The evident differences in accuracy reached by the different schemes indicates the superiority of fifth order methods. Finally, the results using the iterative blast waves [31] are shown in Fig. 1(c) up to $t_{\text{end}} = 0.038$ for 400 cells. These results suggest that the best accuracy among the methods considered is provided by the WENO5Z method, which solves slightly better for the peaks and valleys than the classic WENO5 method. Since this problem does not present analytical solutions, we compare the results for 400 cells with the outcomes of a more accurate calculation, referred to as "exact," obtained using the WENO5 method with 2000 cells.

All the above tests suggest that the methods have been implemented well for the classical one-dimensional Euler set composed of three equations for four unknowns (mass density,
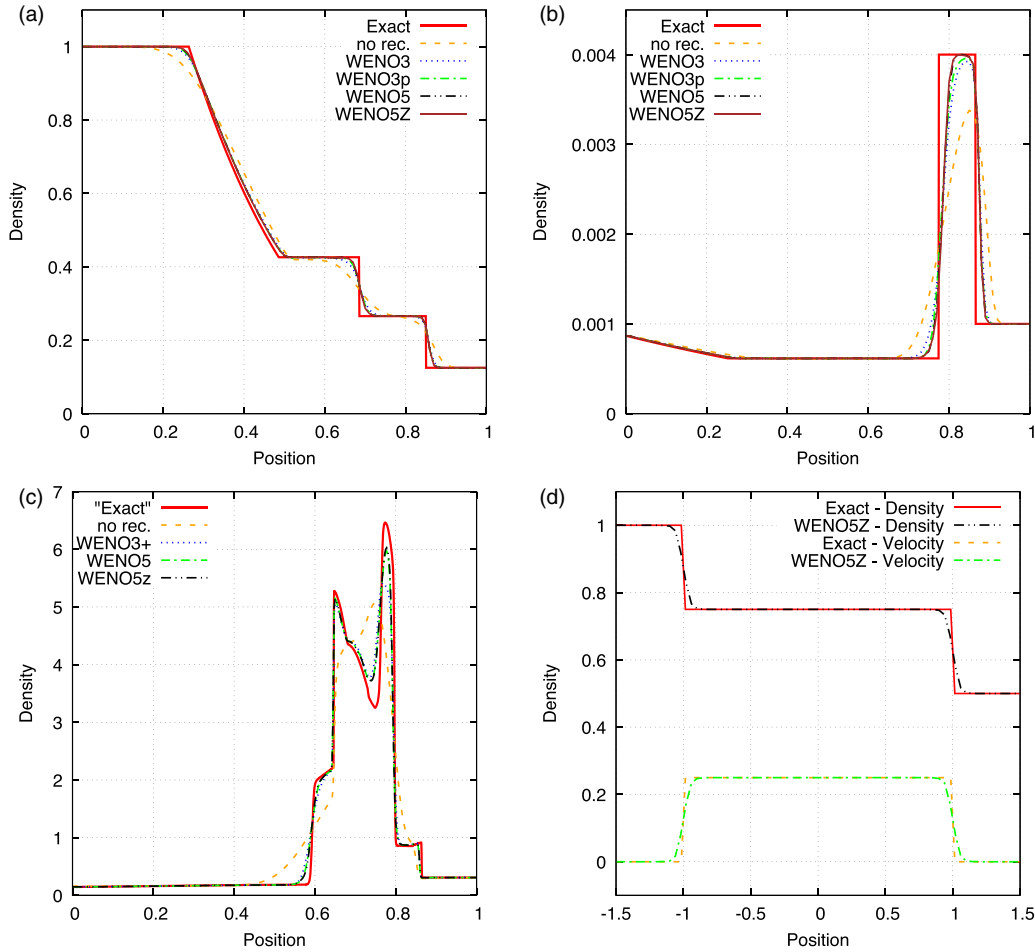
FIG. 1. Density profiles for validation of numerical tests: (a) Sod's problem, (b) blast wave problem, (c) interactive blast waves, and (d) linearized gas.

velocity, pressure, and energy density) which must be complemented with an equation of state providing in this way a relationship among the unknowns. The equations considered in the present work compose a closed set with two equations and two unknowns (the motor and cargo densities), making it possible to perform some simplifications with respect to the application to the Euler problem, in order to improve the computational costs. An additional test applied to the linearized gas dynamics was then performed [32]. This corresponds to a classical Riemann problem with a fluid at rest and density equal to 1.0 on the left-hand side and 0.5 on its right. We then investigate the evolution of the density and velocity profiles of an ideal gas with transmissive boundary conditions. Figure 1(d) shows the results for density and velocity profiles obtained both analytically and also by means of a simulation run for 100 cells using a WENO5Z scheme. The two solutions are in good agreement with each other, even near discontinuities.

IV. DISCUSSION OF RESULTS:
THEORY AND SIMULATIONS

The results presented in the Appendix for the loaded motor density $c(z, t)$, referred to as the cargo density, and for the unloaded motor density $u(z, t)$ are restricted to the perturbative regimes for which both parameter $\frac{\varepsilon}{\gamma} \ll 1$ and $x(z, t)$ and $y(z, t)$ at initial times ($t = 0$) and at the boundary ($z = 0$) also assume small values. The quantities $x(z, t)$ and $y(z, t)$ represent differences in motor and cargo densities with respect to the defined background at $\frac{1}{4}$ in Eq. (A12). However, the results obtained for the two eigenvalues λ_1 and λ_2 in Eq. (A5) are only restricted by the smallness of $\frac{\varepsilon}{\gamma}$. This suggests that the speed of the interface separating the quiet region (QR) from the region Z1, which in the absence of shocks is given by $v_c = \lambda_2(x^*, y^*) \simeq \lambda_2(h, 0)$, can be analyzed for any h within the interval $-\frac{1}{4} < h < \frac{3}{4}$. The parameter h is defined as the excess motor density with respect to the background at initial times (A17). It is then possible to predict that for $|h| \ll 1$ the speed of the interface approaches its maximum value $\lambda_2^{\max} = 0.5$ whereas for $h \sim 0.5$ the speed $\lambda_2(h, 0)$ of the referred interface attains very small values. Therefore, although the expressions derived for λ_1 and λ_2 in terms of the excesses x and y (see the Appendix) do not provide exact results for the speed of the interfaces, especially in cases for which shock and rarefaction of characteristics are determinants of the dynamics, these are useful as guides in our numerical experiments in order to scrutinize the parameter space and investigate the behavior of the quantities of interest.

TABLE II. Analytical and numerical results for density wave profiles and accompanying velocities within the perturbative regime.

Case	h	x_r (10^{-2})	y_r (10^{-2})	v_c $(10^{-1}\ \mu\text{m/s})$	v_{num} $(10^{-1}\ \mu\text{m/s})$	x^* (10^{-2})	y^* (10^{-2})	x^*_{num} (10^{-2})	y^*_{num} (10^{-2})
1	0.01	2.0	−1.0	4.3	4.3	2.0	−1.0	2.0	−1.0
2	−0.01	1.0	−2.0	4.5	4.5	9.0	−1.9	9.0	2.1
3	0.05	0	5.0	5.0	3.9	4.0	−3.0	5.0	0	5.0
4	−0.05	−2.5	−2.5	4.8	4.9	−2.4	−2.4	−2.3	−2.3
5	0.01	0	1.0	4.3	4.3	0	1.0	0	1.0
6	−0.01	2.0	−3.0	4.5	4.5	2.1	−2.1	−1.9	−3.1

The time evolution of motor and cargo density profiles for small values of $|h|$ are expected to display very different shapes compared to those for $h \sim 0.5$. Although we could not predict the fates of the motor and cargo density profiles at these relatively high values of h, we indeed envisioned, on the basis of the results (A19), that the interface separating the QR from its neighboring region might travel at extremely low speeds in comparison to the corresponding speeds at small values of $|h|$. The following examples support these expectations. To ease the access to these studies and for future reference, we compile in Table I the model parameters and main quantities defined in the Appendix.

Cases 1–6 shown in Table II illustrate the behavior of the excess of cargoes and motors for $|h| \ll 1$ at the initial $x_0 = h$ and $y_0 = 0$ and boundary values $x_r = x(0, t)$ and $y_r = y(0, t)$ as indicated. Listed are the speeds of the corresponding interfaces between the QR and Z1 at fixed values $p = 0.9$ (unloaded motor) and $q = 0.85$ (loaded motor). Although other possibilities could be validated, these choices keep the expansion parameter at small values $\frac{2\varepsilon}{\gamma} = 0.06$. The cargo hopping rates between neighbor motors are fixed at $f = g = 0.2$. Setting $f = g$ leads to $\eta = \theta = 1$ (10), which is consistent with the development in Sec. II. The choices for h and boundary values x_r and y_r in each example and the corresponding

numerical v_{num} and predicted (calculated) v_c values obtained using the results in the Appendix are compiled in Table II. The quantity $v_c = \lambda_2(x^*, y^*)$ characterizes the velocity of sharp interfaces between the QR and Z1.

The results for x^* and y^* evaluated with help of the expressions (A24) for $h > 0$ or (A28) for $h < 0$ and the corresponding x^*_{num} and y^*_{num} obtained by numerical simulation for the excess of motors and cargoes within region Z1 are also shown in Table II. Represented in Fig. 2 are the wave density profiles for cases 2 and 3 at different instants of time, as indicated. These are chosen from examples at typical boundary values x_r and y_r and for which the system presents at initial times either slight depletion of motors $h < 0$ or slight excess $h > 0$ with respect to the background at $u = \frac{1}{4}$. The corresponding differences in the average cargo velocities reflect the effects due to motor jamming. The analytical results achieved for the velocities and density profiles are in fact very well represented by their corresponding numerical results. This supports the idea of using these expressions to guide the choice of parameters in order to investigate the behavior of the quantities of interest in axon transport within regions away from the perturbative limits.

Table III shows results from numerical simulation for the speed v_q^p of the wavefront invading the QR as time passes.
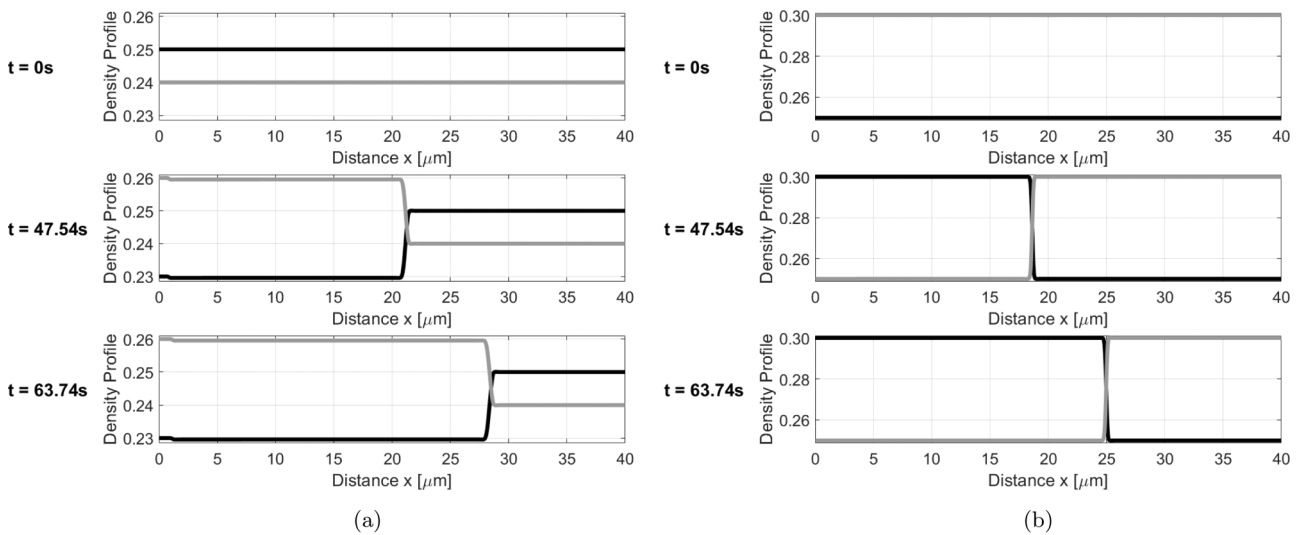

FIG. 2. Time evolution of motor (gray) and cargo (black) density profiles for illustrative examples taken from Table II: (a) case 2, with $x_r = 0.01$ and $y_r = -0.02$, and (b) case 3, with $x_r = 0$ and $y_r = 0.05$. The initial cargo occupation is at $c(z, 0) = 0.25$ and for the scale factor we use $\xi = 1\ \mu$m/s, which sets $\alpha = p$ and $\beta = q$ [see Eq. (10)].

TABLE III. Cargo average velocities v_q^p for motor hopping parameters p (unloaded) and q (loaded) and excess motors on the track h at initial times as indicated, within the nonperturbative regime.

			$h = 0.50$				$h = 0.05$				$h = -0.05$			
			$v_{0.85}^{0.90}$ (nm/s)	$v_{0.25}^{0.90}$ (nm/s)	$v_{0.50}^{0.70}$ (nm/s)	$v_{0.25}^{0.30}$ (nm/s)	$v_{0.85}^{0.90}$ (nm/s)	$v_{0.25}^{0.90}$ (nm/s)	$v_{0.50}^{0.70}$ (nm/s)	$v_{0.25}^{0.30}$ (nm/s)	$v_{0.85}^{0.90}$ (nm/s)	$v_{0.25}^{0.90}$ (nm/s)	$v_{0.50}^{0.70}$ (nm/s)	$v_{0.25}^{0.30}$ (nm/s)
Case	f	g												
1	0.01	0.01	0.6	0.6	0.6	0.6	400.0	120.0	28.0	130.0	490.0	330.0	340.0	160.0
2	0.01	0.20	100.0	74.0	92.0	79.0	420.0	110.0	260.0	110.0	490.0	190.0	320.0	130.0
3	0.20	0.01	8.2	5.6	5.6	24.0	440.0	330.0	330	150.0	520.0	440.0	400.0	130.0
4	0.20	0.20	0.6	0.6	0.6	0.6	400.0	120.0	280.0	130.0	490.0	340.0	360.0	160.0
5	0.20	0.40	110.0	77.0	94.0	81.0	420.0	98.0	260.0	110.0	490.0	180.0	320.0	130.0
6	0.40	0.20	9.0	0.6	7.0	25.0	440.0	340.0	330.0	150.0	520.0	450.0	400.0	170.0

These are indexed by the values for the parameters p and q as shown in each column. We use $(p = 0.9, q = 0.85)$, $(p = 0.7, q = 0.5)$, $(p = 0.2, q = 0.1)$, and $(p = 0.3, q = 0.25)$. These results for v_q^p cannot be reproduced by the expressions derived in the Appendix because the initial and boundary values have been fixed at $h = 0.5$ and at $x_r = -0.1$ and $y_r = 0.1$, respectively, which do not fully satisfy the perturbative conditions. Nonetheless, we expect in these cases that the pulse fixed by the boundary values advancing as a wave profile over Z1 in each case does that at very small velocities, as suggested by the expression for λ_2 in Eq. (A16). The results below illustrating the dependence of v_q^p on the microscopic parameters f and g corroborate these predictions: For large h, i.e., $h = 0.5$, the numerical values depicted for v_q^p are typically orders of magnitude less than the values v_q^p obtained for $|h| = 0.05$. Figure 3 illustrates the corresponding cargo and motor wave density profiles at different instants of time obtained numerically for two situations, case 5 [Fig. 3(a)] and case 6 [Fig. 3(a)], taken from Table III. For certain choices of parameters f and g we compare the numerical results for cargo density profiles for the two initial conditions $h = 0.5$ and $h = -0.05$ at fixed $p = 0.95$ and $q = 0.85$. These results

suggest that associated with the relatively large differences depicted by cargo velocities are large differences from the corresponding wave profile, as observed in experimental data [2].

Table III depicts typical behavior of the average speed v_q^p at which cargoes from the boundary at $z = 0$ advance over the QR. We observe the following.

(i) The average speed v_q^p decreases as the excess of motors h on the track at initial times increases. As h reaches 0.5 and the remaining parameters are kept at fixed values, v_q^p may decrease to such small values up to three orders of magnitude smaller than those reached at $|h| = 0.05$. This is due to an increase of the motor traffic jam that impairs loaded-motor motion through process q. In this case, the important mechanism for driving cargo movement is cargo hopping regulated by rates g (forward) and f (backward). In turn, this may related to the existence of variations in the velocity of slow components that travel on axons known as SCa and SCb, whose speed may differ from each other up to one order of magnitude. These variations are compatible with results in Table III as the parameters g and f change at high values of h.
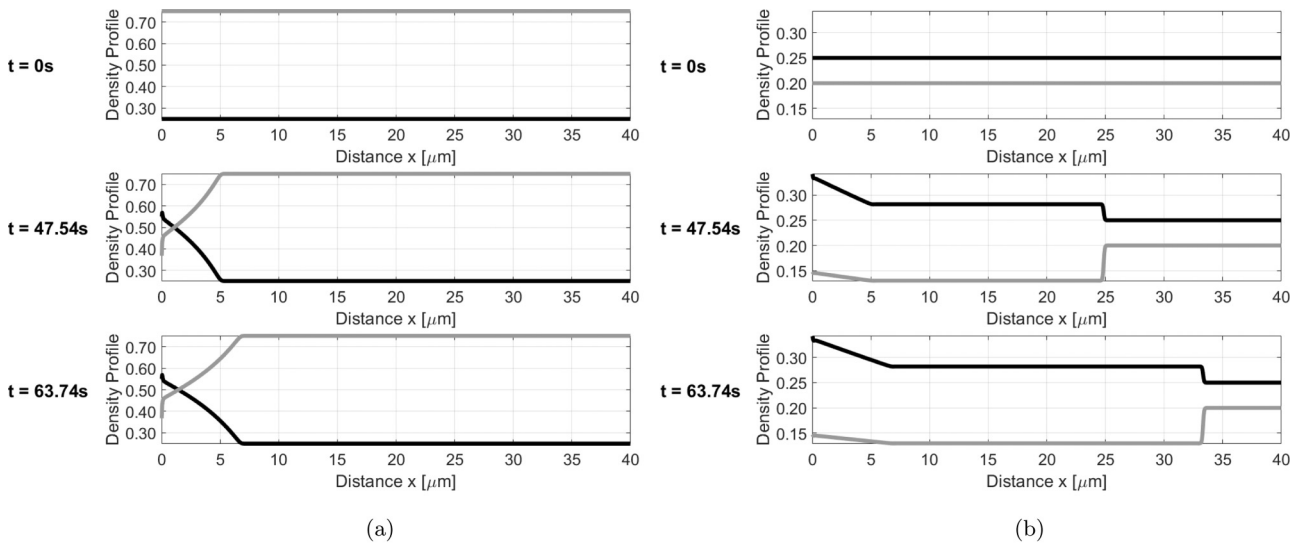

(a)

(b)

FIG. 3. Time evolution of motor (gray) and cargo (black) density profiles for illustrative examples taken from Table III, for $p = 0.90$ and $q = 0.85$ and reservoir excesses $x_r = -0.10$ and $y_r = 0.10$: (a) case 5, with $h = 0.5$, and (b) case 6, with $h = -0.05$. For the scale factor we use $\xi = 1$ μm/s, which sets $\alpha = p$ and $\beta = q$.
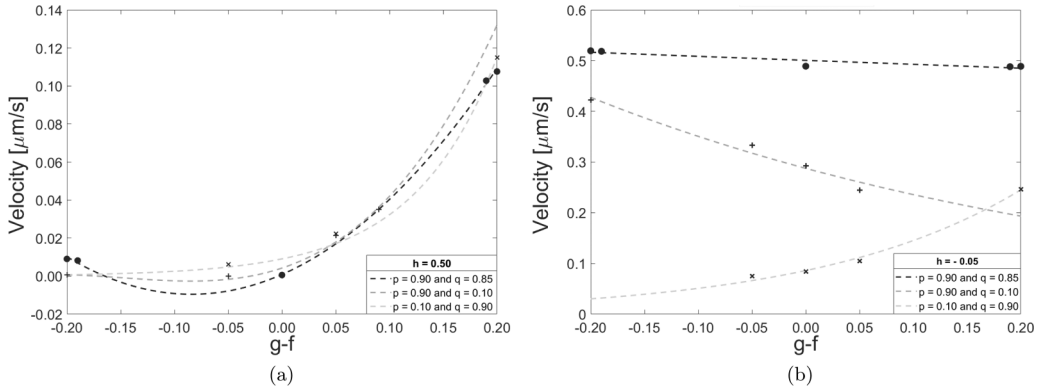
FIG. 4. Behavior of the average cargo velocity with respect to the difference $g - f$ between cargo hopping rates for (a) $h = 0.5$ and (b) $h = -0.05$: $p = 0.1$ and $q = 0.9$ (crosses), $p = 0.9$ and $q = 0.1$ (pluses), and $p = 0.9$ and $q = 0.85$ (circles).

(ii) If $f = g$ and for h not too large, p and q become the dominant processes to drive cargoes. The relatively high values of v_q^p reached at $|h| = 0.05$ (Table III) reflect the success of mechanisms p and q in the absence of a heavy traffic jam (congestion).

(iii) In general, v_q^p increases with the parameters p and q, as expected. However, the effects of increasing p (unloaded motors) and q (loaded motors) in a situation of high motor density should not result in a significant increase of velocities since the traffic jam is the determinant effect in this case, as mentioned. Consistently with this, we expect that the effect of increasing v_q^p with p and/or q will be noticeable at low motor densities, as observed in the results depicted above.

(iv) In connection to (ii) and (iii) above, it is interesting to examine the behavior of average cargo velocity v_q^p with respect to the difference $g - f$ between the two cargo hopping rates. As a general feature, the data in Fig. 4 indicate that at a fixed value of h, the magnitude of v_q^p does not change considerably by changing p or q, at least within the regions of parameters examined. However, there are noticeable changes in the behavior of v_q^p as $f - g$ varies. For $h = 0.5$ and excluding the region for which $g \ll f$, we observe that v_q^p increases with $g - f$ [Fig. 4(a)]. This behavior can be understood since hopping of cargoes among motors is the dominant process for driving cargoes at high motor densities. We should then expect in these situations that v_q^p increases by increasing the forward (anterograde) hopping rate g with respect to f. Figure 4(b) shows that even for small $h = -0.05$ a similar effect may be expected if $p \ll q$. In this case, fast loaded motors may deliver their cargo through process g to the clusters assembled of slow unloaded motors in the front, favoring in this way cargo mobility towards the forward direction as g increases with respect to f. On the other hand, Fig. 4(b) shows also that for $q \ll p$ or $p \gtrsim q$, the average cargo velocity v_q^p decreases as $g - f$ increases. The reasoning for this is that fast unloaded motors would accumulate at the back end of (slow) loaded motors. As f increases with respect to g, cargoes would be more prone to hopping backward to accumulate at the back end of the cluster just formed. This process may create shock waves (of cargoes) whose wavefronts would move rather fast toward the forward direction. A similar effect could be responsible for the decrease of v_q^p for $p \gtrsim q$ and $g \ll f$ shown in Fig. 4(a). We also observe in Fig. 4(b) that for h small, the highest velocities

of the corresponding wave fronts are reached when $p \gtrsim q$, possibly due to a balance among the processes just discussed.

For example, the results achieved here may be related to those reported from experiments performed to investigate the effects of kinesin-binding protein (KBP) on the transport of particles along microtubules [13]. In that study, the authors investigated the effects on particle mobility under variation of the amount of KBP in the systems considered. The effects of increasing KBP have been correlated with a decrease of KIF1A motors attached to the microtubules and with an increase in the average velocities of the remaining moving KIF1A motors after the introduction of KBP. On the contrary, it is observed in another series of experiments that the average velocities of kinesin-based mobile Rab vesicles (cargoes) decrease at increasing KBP (i.e., decreasing the number of motors attached). Figure 5 depicts the predictions of the model for the behavior of average velocities under variations of the excess h for certain choices of parameters, as indicated. Both velocities present a unique global maximum at $h = h_{max}$ that depends on the choices for f and g. This behavior can be understood as resulting from two effects. On the one hand, increasing the excess of motors at low densities ($h < h_{max}$) would contribute to driving the cargoes that are released from the reservoir. On the other hand, effects due to a traffic jam would prevail at large motor densities ($h > h_{max}$), as discussed above. We may then suggest that the data in [13] might be understood as resulting from a balance between these two effects under the condition that the related experiments explore different regions of motor densities.

V. CONCLUSION

Our model describes axon transport of different particles in a unified framework as these are conveyed directly by molecular motors, in the absence of intermediates carriers such as vesicles or any other putative moving structure [4,5]. The idea is that the cargoes are able to detach from molecular motors available on the axon microtubules and attach directly to a neighboring motor according to stochastic processes defined by certain probability rates. These hopping mechanisms are favored under the situation of a heavy traffic jam that leads motors to assemble into large clusters. We propose that such clusters may supply the need for the alleged intermediate
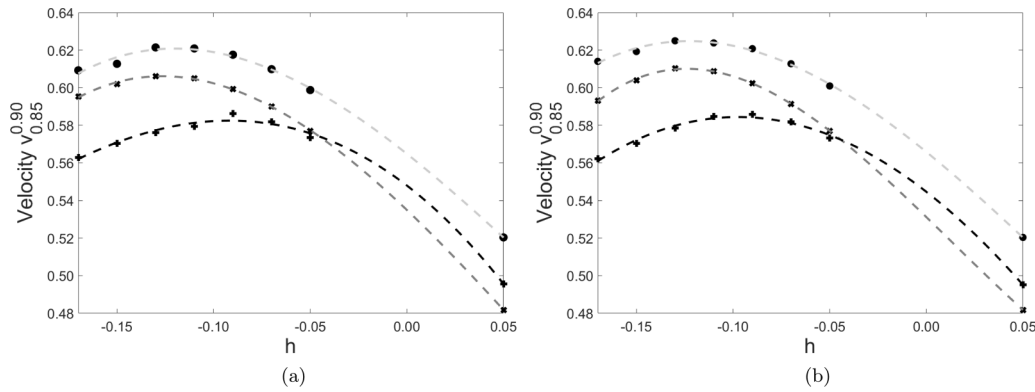
FIG. 5. Variation of the average (a) cargo and (b) motor velocities as the excess motor density h varies, for $c(z, 0) = 0.20$; $p = 0.90$; $q = 0.85$; and $f = g = 0.2$ (crosses), $f = 0.2$ and $g = 0.4$ (pluses), and $f = 0.4$ and $g = 0.2$ (circles).

carriers. The model accounts also for processes leading to direct movement of cargoes attached to motors if allowed by local jamming conditions imposing a steric hindrance. These features are able to predict quantitatively the observed differences between the velocities of the particles conveyed in axons at slow and fast modes, essentially as a consequence of changing the density of motors available because it is the density of motors that regulates the traffic jam. Moreover, the model suggests that the stochastic mechanism of cargo hopping from motor to motor can also explain the differences between the two components displaying slow rates (SCa and SCb) by tuning the corresponding hopping parameters f and g.

In order to be able to extract properties from the model and describe phenomenological aspects of these systems concerning cargo velocities, we have based our analysis on particular solutions to the pair of coupled equations of the Burgers type describing the dynamics of defined densities of motors and cargoes (9). These equations resulted from a mean-field approach of the original stochastic description. We used a perturbative scheme for certain initial and boundary values considering the particular choice for which $f = g$. The analytical solutions to this system of quasilinear partial differential equations achieved in this way indicate the regions of parameters, extending far beyond the perturbative limits, to be investigated numerically in order to obtain information about the system that may relate to the existing data on axonal transport. Such interplay between numerical and analytical approaches has been crucial in exploring the properties of interest.

The description of the interacting particle system considered here allows studying the effects produced by just one kind of carrier motor and one kind of cargo at a time. Also, the model does not take into account explicitly any existing process of motor autoinhibition [33,34] or those due to motor-binding proteins known to participate in the processes to control individual motor mobility on the tracks [13]. Nevertheless, because it is not restricted to any particular set of particles, different motors and cargoes may be taken into account by a separate dynamics characterized by some specific set of parameters. We have presented results for motors that have been chosen possessing anterograde (plus-ended)

bias. These results suggest that cargoes usually recognized as slow components (either SCa or SCb) may also be conveyed in fast-moving modes as already observed, for example, in studies exploring the dynamics of synapsin proteins [35]. According to these predictions, what would determine if a set of cargoes move in a fast or slow mode is a combination of factors comprising their ability to interact with motors and the quantity of motor available on the axon. We leave for future consideration this same kind of description attempting to unravel the corresponding pulselike wave profiles observed in axon transport since these present distinct and typical features for slow and fast components. In addition, future studies may examine the possibility of introducing in this context some effects of controlling motor mobility by autoinhibition and/or the action of external binding proteins.

Finally, we would like to point out that the model encompasses cargo hopping as a one-by-one process through which, at each defined time interval, a single motor may deliver a cargo to a neighboring motor. Experimental data, however, indicate that several motors continuously attaching and detaching from a single cargo are needed to act cooperatively in order to complete each step of the transport process [17]. In view of this, the cargo-hopping model explored here should be seen as an effective model in which the complexity associated with simultaneous interactions of several motors with a single cargo is integrated and replaced by an effective jumping regulated by the rates f and g. In addition to that, we also notice that the mean-field approach overcomes this restriction imposed by the microscopic one-by-one process since the continuum limit eliminates any detail concerning cargo size or the number of motors attached to it at each instant of time, for it introduces the workable concepts of motor and cargo densities. In view of this, we believe that if we had taken into account in the model such details regarding multiple motor interactions with a single cargo, that would not have altered the essence of the results reached here.

APPENDIX: ANALYTICAL SOLUTIONS: COMBINING A PERTURBATIVE APPROACH WITH THE METHOD OF CHARACTERISTICS

The system (9) can be expressed in a vectorial form

$$\frac{\partial U(z,t)}{\partial t} + A(U(z,t))\frac{\partial U(z,t)}{\partial z} = 0, \qquad \text{(A1)}$$

where the vector U is defined by

$$U = \begin{pmatrix} u(z,t) \\ c(z,t) \end{pmatrix} \qquad \text{(A2)}$$

and the matrix A by

$$A = A(U) = \begin{pmatrix} \alpha(1 - 2u - \theta c) & -\alpha\theta u \\ -\beta\eta c & \beta(1 - 2c - \eta u) \end{pmatrix}. \quad \text{(A3)}$$

In order to proceed with a quantitative analysis of Eq. (A1), we examine the case $f = g$, for which $\theta = \eta = 1$. In addition, we parametrize the constants α and β related to the hopping probabilities p and q as

$$\alpha = \gamma + \varepsilon, \quad \beta = \gamma - \varepsilon. \qquad \text{(A4)}$$

We may then express the eigenvalues λ_1 and λ_2 of A in terms of constants γ and ε, which become, for $\frac{\varepsilon}{\gamma} \ll 1$,

$$\lambda_1 \simeq (1 - 2u - 2c)\gamma \left[1 + \frac{\varepsilon}{\gamma}\left(\frac{u-c}{u+c}\right) \right],$$

$$\lambda_2 \simeq (1 - u - c)\gamma \left[1 - \frac{\varepsilon}{\gamma}\left(\frac{u-c}{u+c}\right) \right]. \qquad \text{(A5)}$$

Since λ_1 and λ_2 are distinct from each other and are both real, the system (9) is strictly hyperbolic. Further, λ_1 and λ_2 are related to the velocities of the traveling-wave solutions to Eq. (A1). The corresponding left eigenvectors $\vec{q}_1$ and $\vec{q}_2$ are calculated perturbatively up to first order in the small parameter $\frac{\varepsilon}{\gamma}$, resulting in

$$\vec{q}_1 \simeq \left(-1, \left[-1 - \frac{2\varepsilon}{\gamma}\left(\frac{1-u-c}{u+c}\right) \right] \right),$$

$$\vec{q}_2 \simeq \left(1, \left[-\frac{u}{c} + \frac{2\varepsilon}{\gamma}\frac{u}{c}\left(\frac{1-2u-2c}{u+c}\right) \right] \right). \qquad \text{(A6)}$$

The Riemann invariants $R_1(U)$ and $R_2(U)$ are scalar quantities satisfying $\vec{\nabla} R_i(U) = \vec{q}_i(U)$, $i = \{1, 2\}$ [19,20]. These quantities are conserved by the dynamics along the set of corresponding characteristic curves $z_1(t)$ and $z_2(t)$ defined by $\partial_t z_1 = \lambda_1$ and $\partial_t z_2 = \lambda_2$, that is, λ_1 and λ_2 are the instantaneous velocities at each point of the characteristics on the (z, t) plane. In fact,

$$q_i\left(\frac{\partial U}{\partial t} + \lambda_i \frac{\partial U}{\partial z}\right) = [\vec{\nabla} R_i(U)]\left(\frac{\partial U}{\partial t} + \lambda_i \frac{\partial U}{\partial z}\right)$$

$$= \left(\frac{\partial R_i}{\partial t} + \lambda_i \frac{\partial R_i}{\partial z}\right) \equiv \frac{dR_i}{d\phi_i} = 0, \quad \text{(A7)}$$

where we have used (A1). With regard to the expressions (A5), we observe that if both u and c are constants along the characteristic curves, then both λ_1 and λ_2 are also constants, so the characteristics are straight lines. As indicated in the definition above, the derivative $\frac{d}{d\phi_i}$ is taken along each of the corresponding characteristic curves. Therefore, in order to find R_i, $i = \{1, 2\}$, the expressions (A6) are inserted into the left-hand side of the first equality in the expression (A7) in order to find a general solution R_i by integrating $\frac{dR_i}{d\phi_i} = 0$. For q_1 we obtain the result

$$-\left(\frac{\partial u}{\partial t} + \lambda_1 \frac{\partial u}{\partial z}\right) - \left(\frac{\partial c}{\partial t} + \lambda_1 \frac{\partial c}{\partial z}\right) - \frac{2\varepsilon}{\gamma}\frac{1 - u - c}{u + c}$$

$$\times \left(\frac{\partial c}{\partial t} + \lambda_1 \frac{\partial c}{\partial z}\right) = 0, \qquad \text{(A8)}$$

which can be rewritten as

$$\frac{d}{d\phi_1}\left((1 - u - c) - \ln(1 - u - c) + \frac{2\varepsilon}{\gamma}c \right) = 0, \quad \text{(A9)}$$

where the derivative is taken along the characteristics $\frac{d}{d\phi_1} = \frac{\partial}{\partial t} + \lambda_1 \frac{\partial}{\partial z}$. This means that

$$R_1 = (1 - u - c) - \ln(1 - u - c) + \frac{2\varepsilon}{\gamma}c \qquad \text{(A10)}$$

is the conserved quantity along the set of characteristic curves associated with $q_1(u, c)$. For q_2 we obtain the result

$$c\left(\frac{\partial(u/c)}{\partial t} - \lambda_2 \frac{\partial(u/c)}{\partial z}\right) + \frac{2\varepsilon}{\gamma}\frac{u}{c}\frac{1 - 2(u+c)}{u+c}$$

$$\times \left(\frac{\partial c}{\partial t} + \lambda_2 \frac{\partial c}{\partial z}\right) = 0. \qquad \text{(A11)}$$

In order to write this in a form analogous to (A9) we examine the region of densities for which

$$u(z,t) = \tfrac{1}{4} + x(z,t),$$

$$c(z,t) = \tfrac{1}{4} + y(z,t), \qquad \text{(A12)}$$

with $|x(z,t)|, |y(z,t)| \ll \frac{1}{4}$ representing, respectively, the excess (or depletion) of motors and cargoes at each point of the axon with respect to a considered density "background" set at $\frac{1}{4}$ for both cargoes and motors. With these, Eq. (A11) can be approximated by

$$\frac{d}{d\phi_2}\left(\frac{x + \frac{1}{4}}{y + \frac{1}{4}}\right) \simeq 0, \qquad \text{(A13)}$$

where $\frac{d}{d\phi_2} \equiv \frac{\partial}{\partial t} + \lambda_2 \frac{\partial}{\partial z}$. This yields

$$R_2 \simeq \left(\frac{x + \frac{1}{4}}{y + \frac{1}{4}}\right). \qquad \text{(A14)}$$

For consistency, the expressions for the remaining quantities which are relevant to the analysis that follows must be

reviewed in this region of densities,

$$R_1 \simeq K + x + \left(1 + \frac{2\varepsilon}{\gamma}\right)y, \tag{A15}$$

where $K \equiv \ln 2 + \frac{1}{2} + \frac{1}{4}(\frac{2\varepsilon}{\gamma})$ is a constant. For the eigenvalues,

$$\lambda_1 = \lambda_1(x, y) \simeq -2(x + y)\gamma\left(1 + \frac{2\varepsilon}{\gamma}(x - y)\right),$$

$$\lambda_2 = \lambda_2(x, y) \simeq \left(\frac{1}{2} - (x + y)\right)\gamma\left(1 - \frac{2\varepsilon}{\gamma}(x - y)\right). \tag{A16}$$

Note that the results (A15) for R_1 and (A14) for R_2 are valid as long as $\frac{\varepsilon}{\gamma} \ll 1$ and are restricted to the regions for which $|x(z, t)|, |y(z, t)| \ll \frac{1}{4}$. On the other hand, the results (A16) for λ_1 and λ_2 also need $\frac{\varepsilon}{\gamma} \ll 1$ but are not restricted to the ranges of x and y. We will now use (A14)–(A16) to examine the spatial and temporal behavior of $u(z, t)$ and $c(z, t)$ through the analysis of the characteristic curves for certain initial and boundary conditions.

1. Characteristic lines

We intend to examine the behavior of solutions $c(z, t)$ and $u(z, t)$ for all $z \geqslant 0$ and $t \geqslant 0$ satisfying the pair of equations (9) for initial conditions ($z > 0$ and $t = 0$)

$$c(z, 0) = \frac{1}{4},$$

$$u(z, 0) = \frac{1}{4} + h, \tag{A17}$$

meaning that $x(z, 0) = h$ and $y(z, 0) = 0$ and boundary conditions (at $z \leqslant 0$ and $t \geqslant 0$)

$$c(z \leqslant 0, t) = \frac{1}{4} + y_r, \text{ i.e., } y(z \leqslant 0, t) = y_r,$$

$$u(z \leqslant 0, t) = \frac{1}{4} + x_r, \text{ i.e., } x(z \leqslant 0, t) = x_r. \tag{A18}$$

The constants x_r, y_r, and h are such that $|x_r|, |y_r|, |h| \ll \frac{1}{4}$. Here h represents the excess ($h > 0$) or depletion ($h < 0$) of motor density with respect to the value $\frac{1}{4}$ along the axon at the initial time $t = 0$. The quantities x_r and y_r represent, respectively, the excess or depletion of motors and cargoes in the reservoir at $z \leqslant 0$ and $t \geqslant 0$.

In the following we present a quantitative analysis of the behavior of the two functions $u(z, t)$ and $c(z, t)$ with respect to time at each point of the domain ($z \geqslant 0$) using the method of characteristics. We will restrict this analysis, however, to certain initial and boundary values such that shocks and rarefaction of characteristic lines related to each of the eigenvalues λ_1 or λ_2 would not be relevant up to a first approximation in the small parameter $\frac{\varepsilon}{\gamma}$ to figure out solutions within the time and space domains considered.

As we will see, this approximation is supported by numerical data. Cases for which it does not hold but may be interesting concerning the transport phenomena of interest here are treated numerically and considered afterward for qualitative analysis as an extension of the perturbative results. A quantitative analysis of Eqs. (9) for more general initial and boundary values is not within the scope of the present work.

a. Case h > 0

At $t = 0$ and $z \geqslant 0$,

$$\lambda_1(x(z, 0), y(z, 0)) = \lambda_1(h, 0) \simeq -2h\gamma\left(1 + \frac{2\varepsilon}{\gamma}h\right) < 0,$$

$$\lambda_2(x(z, 0), y(z, 0)) = \lambda_2(h, 0) \simeq \left(\frac{1}{2} - h\right)\gamma\left(1 - \frac{2\varepsilon}{\gamma}h\right) > 0. \tag{A19}$$

We will consider $\frac{2\varepsilon}{\gamma}h \ll 1$. This means that the set of characteristic lines defined as C(I) along which R_1 in (A15) is conserved have negative slope, while the characteristics from the set C(II) along which R_2 in (A14) is conserved have positive slope. Figure 6 suggests that these features may be extended consistently to the solutions $x(z, t)$ and $y(z, t)$ for all $t \geqslant 0$. In fact, notice first that the characteristic $z(t) = \lambda_2(h, 0)t$ from the set C(II) emerging from $z = 0$ divides the plane into two regions. Any point within the region $z(t) > \lambda_2(h, 0)t$, referred to as the quiet region, is reached by characteristics that belong to both sets C(I) and C(II) emerging at $t = 0$ from all points $z \geqslant 0$. The points within the region $z(t) < \lambda_2t$, referred to as region 1 (Z1), are also reached from the set of characteristics C(I) emerging at $t = 0$ from the points $z \geqslant 0$. However, the curves from the set C(II) that reach the points within Z1 are those emerging from the boundary $z = 0$ at $t > 0$. Thus, while the quantities $x(z, t)$ and $y(z, t)$ are resolved within the QR by extending back along both sets of characteristics C(I) and C(II) from any point (z, t) up to the

initial conditions, it happens that within Z1 the corresponding quantities $x(z, t)$ and $y(z, t)$ are resolved extending back from both the initial configuration through C(I) and from the boundary through C(II).

Consider then any point $Q = (z_Q, t_Q)$ at the crossing of two characteristics within the QR, one from the set C(I) and the other from the set C(II). Since the initial conditions are such that both densities are constants for $z > 0$, we may write

$$R_1(z, 0) = K + h = K + x_Q + \left(1 + \frac{2\varepsilon}{\gamma}\right)y_Q,$$

$$R_2(z, 0) = 1 + 4h = \frac{1 + 4x_Q}{1 + 4y_Q}, \tag{A20}$$

where we have defined $x_Q \equiv x(z_Q, t_Q)$ and $y_Q \equiv y(z_Q, t_Q)$. From these two equations, we conclude that at any point Q within the QR, $x_Q = h$ and $y_Q = 0$. This means that the characteristics are straight lines within this region with slopes given in (A19).
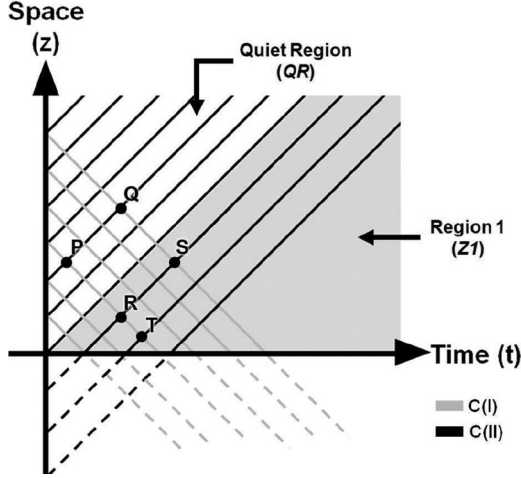
FIG. 6. Characteristic lines for the system (9) with initial and boundary conditions as specified in (A17) and (A18), with $h > 0$.

Consider now the region Z1 defined by the points (z, t) such that $z \leqslant \lambda_2(h, 0)t$, $t > 0$. Figure 6 shows two lines that belong to the set C(I) crossing a line from the set C(II) at points R and S within Z1 and at points P and Q within the QR. It follows that

$$R_2(z_R, t_R) = R_2(z_S, t_S),$$
$$R_1(z_P, t_P) = R_1(z_R, t_R), \qquad (A21)$$
$$R_1(z_Q, t_Q) = R_1(z_S, t_S).$$

Because $y_Q = y_P$ and $x_Q = x_P$ (QR), we conclude that

$$(y_R - y_S)\left(1 + \frac{\varepsilon}{\gamma}\right) = 2(x_S \, y_R - x_R \, y_S), \qquad (A22)$$

which has the trivial solutions $y_R = y_S$ if $x_R = x_S$, implying that the characteristics from C(II) are straight lines within the region Z1. Now, in order to resolve for the quantities $x_+^* \equiv x(z^*, t^*)$ and $y_+^* \equiv y(z^*, t^*)$ at any point (z^*, t^*) of Z1, consider that

$$R_1(0, t) = R_1(z, 0), \qquad (A23a)$$

$$R_2(z^*, t^*) = R_2(0, t), \qquad (A23b)$$

$$R_1(z^*, t^*) = R_1(z, 0). \qquad (A23c)$$

Using the expressions (A14) and (A15), we find that, for the chosen initial and boundary conditions and for $h > 0$, the excesses or depletions of cargoes $y_+^* \equiv y(z^*, t^*)$ and motors $x_+^* \equiv x(z^*, t^*)$ at any point (z^*, t^*) within the Z1 are given by

$$y_+^* = y_r,$$
$$x_+^* = h - \left(1 + \frac{2\varepsilon}{\gamma}\right)y_r. \qquad (A24)$$

With regard to the characteristics C(I) within Z1, we must examine the set of equations relating both quantities $R_1(z, t)$

and $R_2(z, t)$ evaluated at any two points R and T:

$$R_1(z_R, t_R) = R_1(z_T, t_T) = R_1(z, 0),$$
$$R_2(z_R, t_R) = R_2(z_T, t_T) = R_2(0, t). \qquad (A25)$$

The last equality follows from the particular choice of constant boundary conditions as in Eq. (A18). From these we may conclude that $x_R = x_T$ and $y_R = y_T$, meaning that both x and y are individually conserved along the characteristics C(I). In turn, this implies that λ_1 is constant and thus the characteristics of C(I) are also straight lines within Z1. From Eq. (A24) we conclude that for

$$y_r < \frac{h}{\left(\frac{2\varepsilon}{\gamma}\right)} \qquad (A26)$$

the condition $x_+^* + y_+^* > 0$ holds, ensuring that $\lambda_1(x_+^*, y_+^*) < 0$ within Z1, and also that for

$$y_r > \frac{h}{\left(\frac{2\varepsilon}{\gamma}\right)}\left(1 - \frac{1}{2h}\right) \qquad (A27)$$

the condition $\frac{1}{2} - (x_+^* + y_+^*) > 0$ holds, ensuring that $\lambda_2(x_+^*, y_+^*) > 0$ within Z1 so that the characteristics from C(II) have positive slope in this region. These conditions give support to the picture outlined in Fig. 6.

In the forthcoming examples we show that for the initial conditions (A17) with $h > 0$ we can choose values for x_r and y_r for which both $\lambda_1(x, y)$ and $\lambda_2(x, y)$ are approximately conserved within the domain up to the order $\frac{2\varepsilon}{\gamma}$. This means that the characteristic lines from each set C(I) and C(II) are nearly parallel to each other. Therefore, in looking for solutions to $u(z, t)$ and $c(z, t)$ shock formation as well as rarefaction regions can be neglected up to this order of approximation. On the basis of the results discussed above, we conclude that the system evolves in time exhibiting two regions on the (z, t) plane presenting distinct values for the excess of cargoes and motors densities. Within the QR, these quantities preserve their initial values, whereas within Z1, these quantities show also a dependence on the excess of cargoes y_r at the boundary $z = 0$. The speed with which Z1 invades the QR is $\lambda_2(x_+^*, y_+^*)$ (A19). In the present context this characterizes a wave carrying an excess (or depletion) of motors and cargoes that travels toward the positive direction (anterograde transport) along the axon at this speed. We will see next how this picture may change for $h < 0$.

b. Case $h < 0$

In this case we notice that at $t = 0$ both $\lambda_1(h, 0)$ and $\lambda_2(h, 0)$ are positive. We will show that these features are consistent with the solutions $x(z, t)$ and $y(z, t)$ for all time $t > 0$ and space $z \geqslant 0$ domains, as suggested by Fig. 7. In the absence of rarefaction, the characteristics from both sets C(I) and C(II) emerging from $z = 0$ at $t = 0$ divide the plane $z \geqslant 0$ and $t > 0$ into three regions, which will be referred to as the quiet region [upper plane $z(t) > \lambda_2 t$], the intermediate region Z1 [$\lambda_1 t < z(t) < \lambda_2 t$], and the lower region Z2 [$\lambda_1 t > z(t)$].

Like the case $h > 0$, the functions $x(z, t)$ and $y(z, t)$ can be resolved at any point (z, t) within the QR by extending back from (z, t) to the initial values at $t = 0$ along characteristics from both C(I) and C(II) leading to the same equations as in
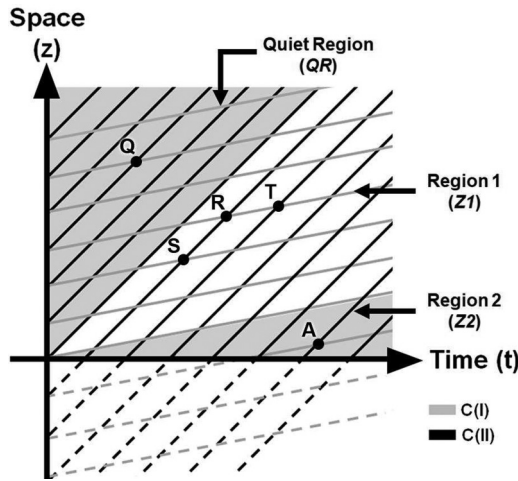
FIG. 7. Characteristic lines for the system (9) with initial and boundary conditions as specified in (A17) and (A18), with $h < 0$.

(A20). This allows us to conclude that both C(I) and C(II) are straight lines and also that $x_Q \equiv x(z_Q, t_Q) = h$ and $y_Q \equiv y(z_Q, t_Q) = 0$ at any point Q within this region.

The analysis of the solutions within the intermediate region (Z1) is performed by choosing any pair of points at the crossing of any two characteristics chosen from the sets C(I) and C(II), say, points R and S, both at the same characteristic of C(II), as shown in Fig. 2. Analogous equations (A21) can be set for these two points, from which we conclude that the C(II) are straight lines within Z1. However, Eq. (A23a), i.e., $R_1(0, t) = R_1(z, 0)$, does not hold in this case. In order to find the solutions x_-^* and y_-^* to x and y for $h < 0$ at any point (z^*, t^*) of Z1, we observe that the set (A25) holds also for $h < 0$, yielding $x_R = x_T$ and $y_R = y_T$ at any two points R and T of a C(I). This implies that λ_1 is also conserved within Z1 and thus the characteristics of C(I) are also straight lines within this region. Equations (A23b) and (A23c) can then be resolved, which yields, in the present case,

$$y_-^* = \frac{1}{4}\left(\frac{(1+4h)(1+4y_r) - (1+4x_r)}{(1+\frac{2\varepsilon}{\gamma})(1+4y_r) + (1+4x_r)}\right),$$

$$x_-^* = h - \left(1 + \frac{2\varepsilon}{\gamma}\right)y_-^*. \tag{A28}$$

The characteristics of C(I) have positive slope, i.e., $\lambda_1(x_-^*, y_-^*) > 0$, at all points within Z1 if $x_-^* + y_-^* = h - \frac{2\varepsilon}{\gamma}y_-^* < 0$. Using the result (A28) for y_-^*, we show that this condition is equivalent to

$$1 + 4y_r > \frac{\frac{2\varepsilon}{\gamma} + 4h}{\frac{2\varepsilon}{\gamma} - 4h}(1 + 4x_r). \tag{A29}$$

Consider now any point $A = (z_A, t_A)$ within Z2, at the crossing of two characteristics, one from the set C(I) and the other from C(II). The quantities $x(z_A, t_A)$ and $y(z_A, t_A)$ are resolved within the Z2 by extending back from (z_A, t_A) along both of these characteristics up to the boundary at $(0, t)$ for any $t \geqslant 0$. Since the excess densities x_r and y_r at the boundary $z = 0$ are kept at constant values as time passes these lead to

$$R_1(z_A, t_A) = R_1(0, t),$$
$$R_2(z_A, t_A) = R_2(0, t). \tag{A30}$$

It follows that

$$x_A = x_r, \quad y_A = y_r \tag{A31}$$

at any point $A = (z_A, t_A)$ within Z2. Both C(I) and C(II) are straight lines within Z2. Moreover, for

$$x_r + y_r < 0 \tag{A32}$$

the signs of both slopes do not change with regard to the other regions, the QR and Z1.

From this analysis we conclude that for $h < 0$ and in the absence of shocks or rarefaction of characteristics, the system evolves in time, exhibiting three regions on the (z, t) plane, each of which present, in the most general case, different values for the excess of cargoes and motors. Within the QR, these quantities preserve their initial values. Within Z1, these quantities show a dependence on both the initial values and the values of excess x_r and y_r at the boundary $z = 0$, as shown in (A30). Within Z2, x and y coincide with their values at the boundaries (A31). Under these conditions, we conclude that the speed at which Z1 invades the QR is $\lambda_2(x_-^*, y_-^*)$. The speed at which the region Z2 invades Z1 is $\lambda_1(x_r, y_r)$.

[1] S. Millecamps and J.-P. Julien, Axonal transport deficits and neurodegenerative diseases, Nat. Rev. Neurosci. **14**, 161 (2013).

[2] S. Roy, Seeing the unseen: The hidden world of slow axonal transport, Neuroscientist **20**, 71 (2014).

[3] M. Tytell, M. M. Black, J. A. Garner, and R. J. Lasek, Axonal transport: Each major rate component reflects the movement of distinct macromolecular complexes, Science **214**, 179 (1981).

[4] J. A. Garner and R. J. Lasek, Cohesive axonal transport of the slow component b complex of polypeptides, J. Neurosci. **2**, 1824 (1982).

[5] Y. Tang, D. Scott, U. Das, D. Gitler, A. Ganguly, and S. Roy, Fast vesicle transport is required for slow axonal transport of synapsin, J. Neurosci. **33**, 15362 (2013).

[6] See, for example, F. Berger, C. Keller, M. J. I. Müller, S. Klumpp, and R. Lipowsky, Co-operative transport of molecular motors, Biochem. Soc. Trans. **39**, 1211 (2011).

[7] J. J. Blum and M. C. Reed, A model for fast axonal transport, Cell Motil. **5**, 507 (1985).

[8] S. Ochs, Characterization of fast orthograde transport, Neurosci. Res. Prog. Bull. **20**, 19 (1981).

[9] A. Brown, Axonal transport of membranous and nonmembranous cargoes: A unified perspective, J. Cell Biol. **160**, 817 (2003).

[10] C. Goldman and E. T. Sena, The dynamics of cargo driven by molecular motors in the context of an asymmetric simple exclusion process, Physica A **388**, 3455 (2009).

[11] C. Goldman, A hopping mechanism for cargo transport by molecular motors on crowded microtubules, J. Stat. Phys. **140**, 1167 (2010).

[12] L. W. Rossi, P. K. Radke, and C. Goldman, Long-range cargo transport on crowded microtubules: The motor jamming mechanism, Physica A **401**, 319 (2014).

[13] J. T. Kevenaar, S. Bianchi, M. van Spronsen, A. Ahkmanova, M. O. Steinmetz, and C. C. Hoogenraad, Kinesin-binding protein controls microtubule dynamics and cargo trafficking by regulating kinesin motor activity, Curr. Biol. **26**, 849 (2016).

[14] A. Kunwar, S. K. Tripathy, J. Xu, M. K. Mattson, P. Anand, R. Sigua, M. Vershinin, R. J. McKenney, C. C. Yu, A. Mogilner, and S. P. Gross, Mechanical stochastic tug-of-war models cannot explain bidirectional lipid-droplet transport, Proc. Natl. Acad. Sci. USA **108**, 18960 (2011).

[15] W. M. Saxton and P. H. Hollenbeck, The axonal transport of mitochondria, J. Cell Sci. **125**, 2095 (2012).

[16] C.-W. Shu, High-order finite difference and finite volume WENO schemes and discontinuous Galerkin methods for CFD, Int. J. Comput. Fluid D **17**, 107 (2003).

[17] L. Conway, D. Wood, E. Tüzel, and J. L. Ross, Motor transport of self-assembled cargoes in crowded environments, Proc. Natl. Acad. Sci. USA **109**, 20814 (2012).

[18] A. Pelizzola and M. Pretti, Cluster approximations for the TASEP: Stationary state and dynamical transition, Eur. Phys. J. B **90**, 183 (2017).

[19] L. C. Evans, *Partial Differential Equations*, 2nd ed. (American Mathematical Society, Providence, 2010).

[20] P. DuChateau, Introduction to nonlinear partial differential equations, https://www.math.colostate.edu/~pauld/M546.html.

[21] W. Zhang and A. I. MacFadyen, RAM: A relativistic adaptive mesh refinement hydrodynamics code, Astrophys. J. Suppl. Ser. **164**, 255 (2006).

[22] J. M. Stone, T. A. Gardiner, P. Teuben, J. F. Hawley, and J. B. Simon, Athena: A new code for astrophysical MHD, Astrophys. J. Suppl. Ser. **178**, 137 (2008).

[23] A. Mignone, P. Tzeferacos, and G. Bodo, High-order conservative finite difference GLM-MHD schemes for cell-centered MHD, J. Comput. Phys. **229**, 5896 (2010).

[24] J. M. Martí and E. Müller, Numerical hydrodynamics in special relativity, Liv. Rev. Relativ. **6**, 7 (2003).

[25] D. S. Balsara and C.-W. Shu, Monotonicity preserving weighted essentially non-oscillatory schemes with increasingly high order of accuracy, J. Comput. Phys. **160**, 405 (2000).

[26] G.-S. Jiang and C.-W. Shu, Efficient Implementation of weighted ENO schemes, J. Comput. Phys. **126**, 202 (1996).

[27] N. K. Yamaleev and M. H. Carpenter, Third-order energy stable WENO scheme, J. Comput. Phys. **228**, 3025 (2009).

[28] R. Borges, M. Carmona, B. Costa, and W.-S. Don, An improved weighted essentially non-oscillatory scheme for hyperbolic conservation laws, J. Comput. Phys. **227**, 3191 (2008).

[29] S. Gottlieb, D. I. Ketcheson, and C.-W. Shu, High order strong stability preserving time discretizations, J. Sci. Comput. **38**, 251 (2008).

[30] G. A. Sod, A survey of several finite difference methods for systems of nonlinear hyperbolic conservation laws, J. Comput. Phys. **27**, 1 (1978).

[31] P. Woodward and P. Colella, The numerical simulation of two-dimensional fluid flow with strong shocks, J. Comput. Phys. **54**, 115 (1984).

[32] E. F. Toro, *Riemann Solvers and Numerical Methods for Fluid Dynamics* (Springer, Berlin, 2009).

[33] J. W. Hammond, D. Cai, T. L. Blasius, Z. Li, Y. Jiang, G. T. Jih, E. Meyhofer, and K. J. Verhey, Mammalian kinesin-3 motors are dimeric in vivo and move by processive motility upon release of autoinhibition, PLoS Biol. **7**, e1000072 (2009).

[34] K. J. Verhey and J. H. Hammond, Traffic control: Regulation of kinesin motors, Nat. Rev. Mol. Cell Biol. **10**, 765 (2009).

[35] D. A. Scott, U. Das, Y. Tang, and S. Roy, Mechanistic logic underlying the axonal transport of cytosolic proteins, Neuron **70**, 441 (2011).